Phase transformations and magnetostriction in Fe100-xGax bulk alloys

Phase transformation and magnetostriction in $Fe_{100-x}Ga_x$ bulk alloys

Marco Coïsson1,_ Kouassi Dakmak N'Dri2, Lindor Diallo3, Elena S. Olivetti1, Luca Martino1, Carlo P. Sasso1, Federica Celegato1, Gabriele Barrera1, Massimo Pasquale1, Paola Rizzi3, Mery Malandrino3, Olha Nakonechna4, Paola Tiberto1, Jean Juraszek4, Saïda Bahamida5, and Abdeslem Fnidiki4

1INRIM, Advanced Materials and Life Sciences Division, Torino, Italy
2Faculty of Science and Technology, University of Lorraine, France
3University of Torino, Chemistry Department, Torino, Italy
4Normandie University, UNIROUEN, INSA Rouen,
CNRS, GPM, 76000, Rouen, France and
5University of Boumerdes, 35000 Boumerdes, Algeria

J. Appl. Phys. 132, 183912 (2022);

doi: 10.1063/5.0097930

Phase transformation and magnetostriction in $Fe_{100-x}Ga_x$ bulk alloys

Marco Coïsson[1],* Kouassi Dakmak N'Dri[2], Lindor Diallo[3], Elena S. Olivetti[1], Luca Martino[1], Carlo P. Sasso[1], Federica Celegato[1], Gabriele Barrera[1], Massimo Pasquale[1], Paola Rizzi[3], Mery Malandrino[3], Olha Nakonechna[4], Paola Tiberto[1], Jean Juraszek[4], Saïda Bahamida[5], and Abdeslem Fnidiki[4]

[1] *INRIM, Advanced Materials and Life Sciences Division, Torino, Italy*

[2] *Faculty of Science and Technology, University of Lorraine, France*

[3] *University of Torino, Chemistry Department, Torino, Italy*

[4] *Normandie University, UNIROUEN, INSA Rouen, CNRS, GPM, 76000, Rouen, France and*

[5] *University of Boumerdes, 35000 Boumerdes, Algeria*

* m.coisson@inrim.it

ABSTRACT

Fe-Ga alloys, containing 18, 21 and 23 at.% of Ga, were prepared in bulk form. In their as-cast state they display a small magnetostriction, that is strongly improved after annealing at 1000 °C for 24 h, and subsequent rapid cooling. Multiple characterisation techniques, such as X-ray diffraction, differential scanning calorimetry, Mössbauer spectroscopy, temperature-dependent magnetisation curves, hysteresis loops, magnetic force microscopy and magnetostriction measurements were exploited in synergy to gain a deep understanding of the structure-properties relationships in the studied alloys, before and after annealing. The A2 phase, which is favoured in the lower range of compositions and is promoted at the expense of the $D0_3$ one by the annealing, is responsible for characteristic dendritic and maze magnetic domains, and for the strong improvement of the magnetostriction, which almost reaches 240 ppm (transverse configuration) in the alloys with 18 at.% of Ga, after annealing.

I. INTRODUCTION

Large magnetostriction and magnetoelastic coupling are properties extensively sought after because of their exploitability in low power consumption devices [1, 2], energy conversion [3], and spintronics [4, 5]. Many alloys displaying large magnetostriction coefficients contain rare earths [6], whereas Fe-Ga systems, being rare earths free, have attracted attention because of their significant magnetostrictive response, coupled with good corrosion resistance and mechanical hardness [7].

Magnetostriction is particularly significant in Fe-rich alloys, with Ga content approximately equal to 19% and 27% [7, 8]. In this range of compositions, the Fe-Ga binary system is characterised by the possible presence of multiple phases [9–12], whose complex interplay strongly affects the magnetostrictive response. The stabilisation of the A2 or $D0_3$ phases by means of additional species in the alloy, like Tb [13–15] or Ce [16], turned out to be particularly effective to enhance magnetostriction, but partially defeats the purpose of getting rid of rare earths. However, a careful tailoring of the alloy microstructure can also lead to remarkable magnetostrictive properties [17], as well as the development, in thin films, of an ordered crystal growth on Si, MgO or GaAs substrates [18, 19], of 6 layer modulated monoclinic phases at the boundaries of the dominant bcc phase [20], of Ga-Ga pairs in the

A2 phase [21], or even of a polycrystalline, non oriented, dominant $D0_3$ phase, in spite of its tendency to minimise the Ga-Ga pairs [18, 21–23].

Despite the Fe-Ga binary system is studied since many decades, its equilibrium phase diagram is still under assessment. Recently, Mohamed et al. [24] proposed a revisited version of the Fe-rich side of the phase diagram by comparing four different previous versions with their experimental data about a considerable amount of compositions, suggesting that some phase boundaries should be shifted. Besides, one should consider that in as-cast samples equilibrium conditions are rarely attained and the presence of quenched metastable phases should always be considered. Thus, a metastable phase diagram such as the one in [9] is often more appropriate in determining the sample phase composition and transformations. In addition, as will be discussed later, distinguishing between the disordered A2 and the ordered $D0_3$ phase is extremely difficult and requires sophisticated characterisation techniques, such as SAED [25] or high energy X-ray diffraction [26]. For these reasons, since the magnetostrictive properties are strictly dependent on the phase composition and stability, studies aiming at contributing to a comprehensive assessment of the structure-properties relationships in the Fe-Ga alloy system are particularly valuable.

Within this context, the present work performs a detailed study on the microstructure and on the magnetic and magnetostrictive properties of $Fe_{100-x}Ga_x$ (with $x = 18$, 21 and 23) bulk alloys, through a combination of multiple techniques, including X-ray diffraction, conversion electron Mössbauer spectroscopy, differential scanning calorimetry, thermomagnetic curves, hysteresis loops, magnetic force microscopy and magnetostriction measurements. The chosen compositions cover an interval centred around $19 - 21$ at.% where the best magnetostrictive response is supposed to be found. The samples were also submitted to thermal treatments and rapid cooling to promote the development of the A2 phase. The complementary information provided by these multiple techniques helps in clarifying the complex metastable Fe-Ga phase diagram in the studied Ga range, and gives a comprehensive description of the phases present in the different alloys and of how they transform upon heating, making possible a direct relationship between microstructure and magnetic properties, magnetic domains configuration and magnetostriction.

II. MATERIALS AND METHODS

$Fe_{100-x}Ga_x$, with $x = 18, 21, 23\%$ at. Ga, master alloys were prepared by electric arc melting. Their composition was determined through semi-quantitative energy-dispersive X-ray spectroscopy (EDX) analysis on a SEM-FEG (FEI Inspect-F) using a standardless ZAF matrix correction routine. The samples were labelled as Ga18, Ga21 and Ga23 respectively. While EDX may not be very accurate, in our case the reported compositions matched well with those expected from saturation magnetisation measurements (see Table III later in the text). In any case, the samples compositions was also checked using two additional independent methods.

For the first, selected portions of the three samples were dissolved using acid digestion in a microwave oven (Milestone MLS-1200 MEGA). Sample aliquots were treated with 5 mL of aqua regia in tetrafluoromethoxyl (TFM) bombs. Four heating steps of 5 min each (250, 400, 600, 250 W power respectively), followed by a ventilation step of 25 min, were applied. At the end of the full treatment, the samples appeared completely dissolved. Subsequently, the resulting solutions were diluted to 20 mL with highly purified water. A further dilution (1:50) was necessary as a final step to determine Fe and Ga concentrations by inductively coupled plasma - optical emission spectroscopy (ICP-OES, Optima 7000 DV Perkin Elmer) equipped with a PEEK Mira Mist nebuliser, a cyclonic spray chamber and an Echelle monochromator. The wavelengths were 238.204 and 417.206 nm for Fe and Ga respectively. Each concentration value was averaged on the basis of three instrumental measurements. Using this technique, the Ga content turned out to be 17.3 at.% for Ga18, 19.3 at.% for Ga21 and 20.9 at.% for Ga23 samples respectively, therefore slightly poorer in Ga with respect to the composition determined by EDX.

For the second, the atom probe tomography (APT) was used to investigate the redistribution of Ga in the Ga21 alloy. Two specimens for APT measurements were prepared by the standard electropolishing method [27, 28] using the Ethanol/Perchloric acid electrolyte in 75/25-vol.%, 90/10-vol.%, and 95/5-vol.%. The atom probe analyses were performed on a CAMECA LEAP 4000 HR, at 50 K, with a pulse fraction of 20% and repetition rate of 200 kHz, with a detection rate of 0.15%. The data were processed using IVAS®3.6.8. software [27, 29]. An example of the 3D reconstruction maps of the analysed volumes for Ga (shown in purple) and Fe (shown in black) atoms are shown in Figure 1. For both samples

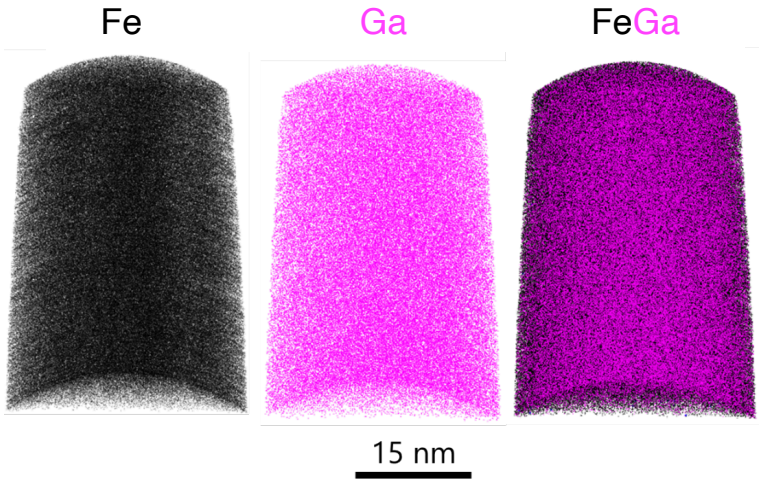

FIG. 1. 3D reconstruction of Ga (purple) and Fe (black) atoms in a Ga21 sample volume analysed by atom probe tomography.

three analyses have been conducted, and the Ga atoms were homogeneously distributed in the analysed volume. The sample shown in Figure 1 turned out to be constituted by 21.3 at.% of Ga, whereas the other sample contained 20.4 at.% of Ga, in excellent agreement with the composition determined by EDX and inductively coupled plasma-optical emission spectroscopy. For simplicity, the composition determined by EDX (Ga18, Ga21 and Ga23) will therefore be retained for the subsequent discussion.

The raw ingots had a typical size of the order of 6 x 5 x 4 cm^3, and were tempered in water. The cooling rate is known to significantly affect the microstructure [30], but in ingots of this size it is extremely difficult to control the cooling rate and to ensure that it is homogeneous in the whole ingot volume. Therefore, in the case of the as-cast samples, a non-homogeneous microstructure is expected. The samples were cut with diamond wire to obtain parralepiped-shaped samples $\approx$ 1 mm thick. Finally, they were mirror-polished with diamond paste (final polish 0.25 μm). In order to promote both homogenisation of the microstructure and phase transformations, selected samples for each composition were furnace annealed in vacuum (base pressure $1 \cdot 10^{-6}$ mbar) at 1000 °C for 24 h, in a quartz tube. After the annealing, they were cooled to room temperature by removing the quartz tube from the furnace, ensuring an initial average cooling rate of $\approx$ 150 °C/min down to 500 °C, followed by an average cooling rate of $\approx$ 40 °C/min down to 300 °C. These cooling rates should be fast enough to minimise the development of the $L1_2$ phase at the expense of

the $D0_3$ one [31].

X-ray diffraction analysis (XRD) was conducted at room temperature with a Panalytical X'Pert Pro diffractometer in the Bragg-Brentano configuration (Cu radiation, $\lambda = 0.15418$ nm) on polished samples. Since the XRD patterns of the A2, B2 and $D0_3$ phases were not available in the databases, the unit cells of the disordered and ordered phases of interest were built by means of the free software Vesta [32] using space groups and lattice parameters data reported in [10] and their diffraction patterns calculated with the same software and used as a reference to index peaks in the experimental patterns.

Structural and magnetic phase transition temperatures were determined by differential scanning calorimetry (Pyris Diamond DSC, PerkinElmer) with a heating and cooling rate of 5 °C/min within a temperature range from 25 to 725 °C. The measurements were done under an Ar flow of approximately 20 ml/min. Each sample was subjected to two thermal cycles of heating and cooling in order to distinguish reversible transformations (e.g. Curie transition, equilibrium phase transformations) from irreversible ones (e.g. metastable phase transformations). The heat flux of the empty copper crucible recorded in the same measurement conditions was subtracted from the heat flux of each sample to get rid of the baseline contribution to the measured signal, due to instrumental factors and to a slight oxidation of the copper itself.

Mössbauer Spectroscopy, performed at room temperature, was also exploited to identify the different phases present in the samples by properly evaluating the parameters resulting from the hyperfine interaction (the hyperfine field B_{hf} and the isomer shift δ). The CEMS technique (Conversion Electron Mössbauer Spectroscopy) has a penetration depth of about $80 - 100$ nm, and is therefore useful for analysing the near surface region [33, 34] of the samples. CEMS experiments were performed at room temperature and in normal incidence by using a He-CH_4 gas flow proportional counter [35]. The radioactive source was ^{57}Co in a rhodium matrix with an activity of $\approx$ 1.5 GBq, moved in constant acceleration mode. Magnetic CEMS spectra were fitted with a discrete distribution of hyperfine fields B_{hf} with a least-squares procedure [36]. A correlation between hyperfine field and isomer shift δ was used to take into account the Fe environment distribution [37–40]. δ values at the ^{57}Fe nuclei are given relative to α-Fe at room temperature. Estimated errors for the hyperfine parameters originate from the statistical errors σ given by the fitting program, taking a confidence value of 3 (i.e. 3σ).

For magnetic characterisations, the samples were cut into approximately 2 mm x 2 mm x 1 mm pieces to be fitted into a vibrating sample magnetometer (VSM, LakeShore 7410). Hysteresis loops were measured at room temperature, whereas magnetisation *vs.* temperature was measured up to 680 °C under an applied field of 500 Oe (50 mT). Saturation M_S, remanence M_r and coercivity H_c have been extracted from hysteresis loops data, whereas Curie temperatures T_C were obtained from temperature-dependent curves.

Additional magnetic characterisations were performed by magnetic force microscopy (MFM, Bruker Multimode V) exploiting Co-Cr coated Si tips (Bruker MESP-HR) in intermittent-contact lift mode with a typical lift scan height of 50 nm. The tips were magnetised along their axis. The samples were analysed by MFM at their in-plane magnetic remanence state. In the MFM, in addition to the height channel (AFM), the magnetic information was obtained through the phase channel in pass 2.

The samples used for magnetostriction measurements were cut into pieces having a size of $\approx$ 10 mm x 6 mm x 1 mm. Strain gauges with a resistance of $\approx$ 120 Ω were glued with epoxy resin on the samples surface, and the measurements were made at room temperature by a Wheatstone bridge under an applied magnetic field aligned along the 6 mm side of the sample. The measurements were performed by aligning a saturating magnetic field (10 kOe = 1 T) along the 6 mm edge, then by rotating the sample by 90° under the same saturating field (now aligned to the 10 mm side). The value $\Delta\lambda$ representing the difference of the reading of the strain gauge in the two configurations allows to calculate the saturation magnetostriction value according to the expression $\lambda_s = \frac{2}{3}\Delta\lambda$ [41].

III. RESULTS AND DISCUSSION

In the region the phase diagram [9] relevant for the present study, i.e. the portion with the Ga content within 18 and 23 at.%, the equilibrium phases are the A2 disordered bcc structure and the $L1_2$ fcc superlattice. However, the bcc-ordered phases B2 and $D0_3$ can be quenched at room temperature due to the slow kinetics of phase transformation [9, 30]. As a matter of fact, several authors [24, 30] report that as cast Fe-Ga alloys usually present a metastable structure, dependent on the Ga content: for Ga $< 20\%$ only the A2 phase is present, whereas for Ga between 20 and 27% $D0_3$ clusters of increasing size [30] are observed embedded in the A2 matrix.

The identification of ordered and disordered FeGa phases through standard laboratory X-ray diffraction is a difficult task, since the superlattice lines, produced by atomic ordering, are very weak and difficult to detect since Fe and Ga have similar atomic number (Z = 26 and 31, respectively) and hence similar scattering factors [26, 42]. In addition, the fundamental lines of bcc-derived phases appear at very similar angular positions since the atomic ordering does not produce appreciable changes in lattice parameters. Peak splitting of high angle reflections (e.g. (220)) has been used in addition to superlattice lines as a tool to detect two-phase mixtures of A2 and $D0_3$ [43], however this approach requires high resolution diffractometers and small peak FWHM. Figure 2 shows the calculated XRD patterns of the disordered A2 phase and of the three ordered phases of interest (B2, $D0_3$ and $L1_2$). The patterns were generated by building the unit cells of each phase (displayed on the right of Figure 2) with Vesta free software [32] using the lattice parameters reported in [10] for the following compositions: $Fe_{80}Ga_{20}$ (A2), $Fe_{75}Ga_{25}$ ($D0_3$ and $L1_2$), and $Fe_{61}Ga_{39}$ (B2). As one can see, the patterns of all the bcc phases are very similar, differing only for the presence of low intensity reflections due to atomic ordering in a superlattice.

X-ray diffractograms of the as-prepared and annealed samples are reported in Figure 3. The Ga18 sample is essentially a single phase material with an A2 disordered structure. In this sample, only minimal traces of peaks attributable to $L1_2$ phase are visible. After the heat treatment at 1000 °C no substantial change in peak positions of the A2 phase has been observed. On the other hand, the minor peaks of $L1_2$ were not detected, although they might have been missed owing to the lower overall intensity of the annealed sample pattern due to the reduced sample size of the annealed specimen. In the XRD pattern of the as-cast Ga21 sample, a weak superlattice line is visible at low angles, revealing that this sample may contain a certain proportion of ordered bcc phase (either B2 or $D0_3$) embedded in the A2 matrix, together with the $L1_2$ fcc ordered phase. After annealing at 1000 °C, both the superlattice lines and the $L1_2$ peaks disappeared, leaving a single phase material with peaks shifted toward higher angles, indicating a decrease in lattice parameter of the cell possibly due to a phase transformation from $D0_3$/B2 structure to A2 structure [43]. The main peaks of sample Ga23 are well matched by the reflections of the $D0_3$ ordered phase, since, in addition to a weak superlattice line at low angle, other lines unique to this phase are visible around $2\theta \approx 105°$. The appearance of these reflections at high angle and, more generally, the deviations of relative intensities from the ones expected for a random powder, observed

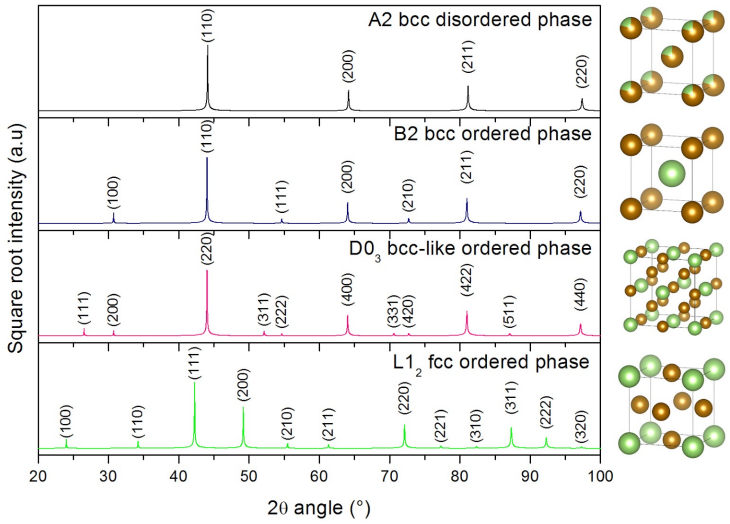

FIG. 2. Comparison of calculated XRD patterns of the ordered and disordered phases in the Fe-rich region of the Fe-Ga phase diagram ($\lambda = 1.54059$ Å). The square root of intensities is presented to better display the low-intensity superlattice reflections due to atomic ordering. The unit cell of each phase is represented on the right (not-to-scale). Green spheres represent Ga atoms, brown spheres Fe atoms, while double-coloured spheres represent positions where either Fe or Ga atoms can be present.

in all the samples, are likely due to the coarse grain size of the alloy ($400 - 700$ μm), that causes only a few crystals to diffract, especially at high angles. As in previously described samples, the disordered A2 phase cannot be excluded: indeed, at a closer inspection, the peaks of the fundamental lines appear quite asymmetrical with a shoulder on the low angle side of the profile, possibly revealing the coexistence of different phases with the same crystal structure but slight differences in lattice parameters. Upon annealing, the reflections of the $D0_3$ phase disappear. In addition, the peaks of the $L1_2$ phase are detectable both in the as cast and in the annealed state.

In general, therefore, the studied samples in the as-cast state follow the behaviour already observed by other studies [26], where faint superlattice lines were observed starting for alloys with Ga at.% greater than 21% [44], revealing that the out-of-equilibrium solidification conditions were able to quench a certain amount of the ordered phase stable at temperatures > 588 °C, whereas after annealing, the $D0_3$ phase, when present in the as-cast samples,

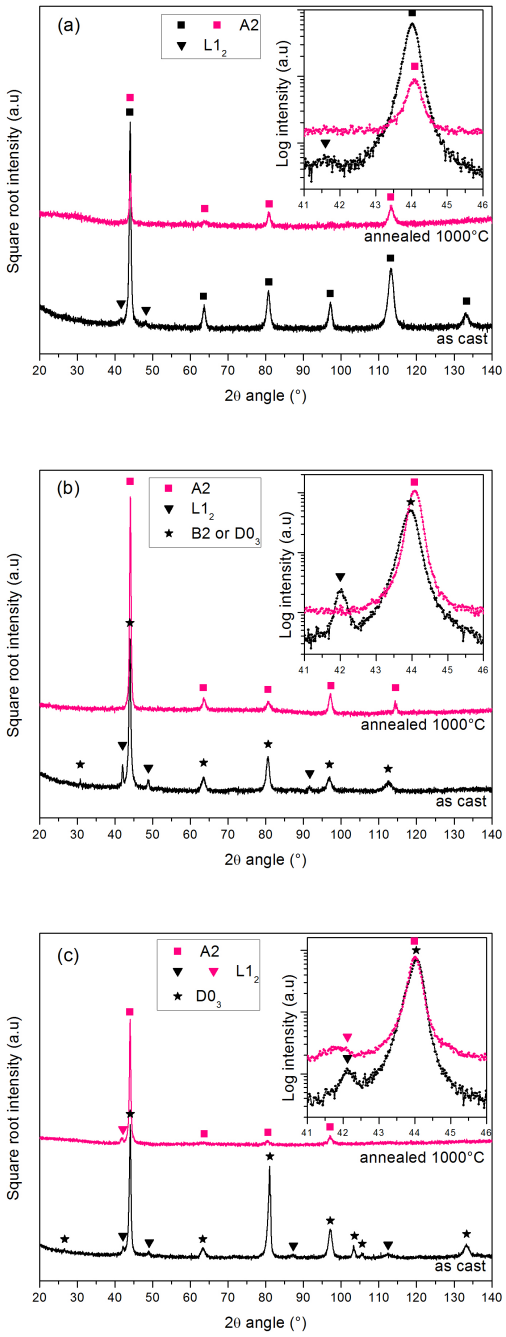

FIG. 3. Diffractograms of the $x = 18$ (a), 21 (b) and 23 (c) at.% Ga samples, as-cast and annealed. Patterns have been vertically translated for a better evaluation of the details.

transforms into the A2 one, eventually disappearing as expected owing to its metastability at room temperature.

Mössbauer spectroscopy (Figure 4) gives a direct link between the samples crystal structure and their magnetic properties, as it is sensitive to the environment in which the Fe atoms are placed. All spectra reported in Figure 4 for the as-prepared samples display a sextet, typical of ferromagnetic behaviour, with relatively large peaks, suggesting a disordered crystal structure, which evolves into a slightly more ordered one (narrower peaks) as the Ga content is increased. All three compositions show a peak of the hyperfine field distribution around 300 kOe (30 T), attributed to a Fe-rich phase. As the width of the peak is rather large, this phase must be disordered; therefore this peak can be assigned to the A2 phase. The fit was improved by adding a paramagnetic quadrupolar doublet with quadrupole splitting value of about 1.2 mm/s, assigned to a minority phase, not detected by XRD. The relative spectral area of this paramagnetic minor phase increases with Ga content. This paramagnetic contribution is attributed to a Ga-rich phase. The average hyperfine field value decreases with Ga content, as reported in Table I and in agreement with literature [45]. Average values of the isomer shifts do not show a significant variation within this small range of compositions. However, the highest value of $< \delta >$ is obtained for the Ga23 sample, in agreement with an increase of isomer shift with Ga content reported in the literature [45, 46].

TABLE I. Average values of hyperfine field $< B_{hf} >$, isomer shifts $< \delta >$ and spectral area A_p of the paramagnetic phase, deduced from the fit of the Mössbauer data of the Ga18, Ga21 and Ga23 as-prepared samples.

Ga%	$< B_{hf} >$ (kOe)	$< B_{hf} >$ (T)	$< \delta >$ (mm/s)	A_p %
18	281	28.1	0.19(3)	4
21	279	27.9	0.18(7)	6
23	258	25.8	0.20(3)	9

Complementary information comes from differential scanning calorimetry, which is able to detect phase transformations occurring as a function of temperature. Table II lists the magnetic and structural transformations possible in the Fe-Ga alloys of selected composi-

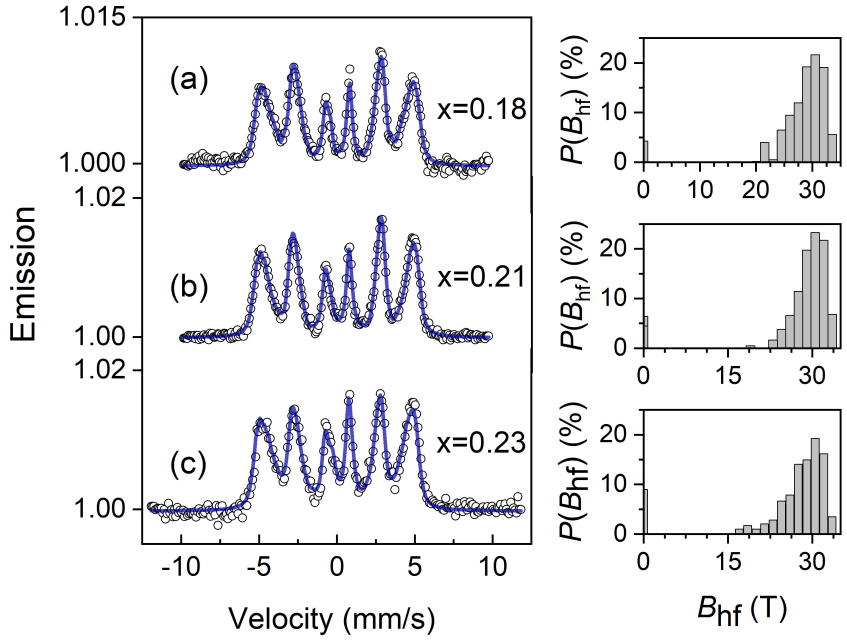

FIG. 4. CEMS spectra at room temperature and corresponding hyperfine field distributions of the Ga18 (a), Ga21 (b) and Ga23 (c) alloys.

tions, whereas Figure 5(a) displays the DSC traces of the as-cast samples. For each sample the first heating and first cooling curves are reported to evaluate the reversibility of the observed signals. The signal derivatives are reported in panel (b) to better detect the small changes observed mainly in a region of rapid variation of the baseline signal. For sample Ga18, only the FM $\rightarrow$ PM transition [t18-1] is expected within the temperature range of the DSC (see Table II); as a mater of fact, there are no significant features highlighted by the DSC curve, considering that even its derivative signal is completely flat in the high temperature region shown in Figure 5(b): this is in agreement with XRD data, since this sample is mainly composed of stable phases (A2 and $L1_2$). As a general rule, the Curie temperatures of all Fe-Ga magnetic phases decrease with increasing Ga content, with a steep decrease in the range of Ga 15-25 at.% [45]. An increase of the Curie temperature could appear only if large amounts of the $L1_2$ phase were present, which is not our case. According to available literature data [9], the A2 phase should have a Curie temperature within the DSC measurement range for Ga $>$ 18 at.%. However, since the heat capacity change associated with magnetic transitions is very small (roughly 0.1 $Jg^{-1}{}^{\circ}C^{-1}$) [47], Curie temperature is

often missed by conventional DSC measurements, because its signal can be lost in baseline curvature and related DSC cell effects. Samples Ga21 and Ga23, instead, display a richer set of possible transformations upon heating (see Table II) and show clear peaks in the high temperature range of the DSC measurement, especially evident in the cooling curves, thus related to reversible phenomena. However the exact attribution of the observed signals to a particular physical process is difficult, owing to the complexity of the multiphase system and to the subtle differences between the phases.

In the DSC traces of sample Ga21, only two of the five predicted events are detected: the heating curve has extremely faint variations in the steep descendent portion, but looking at the derivative two minima are apparent, that seem to indicate two distinct processes occurring at close, but different temperatures: namely 645 °C and 660 °C. This is qualitatively consistent with the observed thermomagnetic behaviour, although temperature differences are observed between calorimetric and magnetic data for the event at lower temperature. The same features have been observed in the second heating and second cooling runs (not shown) as well, indicating a fully reversible thermal behaviour.

Ikeda et al. [9] have performed DSC experiments on Fe-Ga alloys of a composition (Ga 21.5 at.%) similar to ours: they observed three signals that were attributed to processes [t21-1], [t21-2] and [t21-4] mentioned in Table II, although the signal of process [t21-1] was quite faint and they did not consider the possible transformations of $L1_2$ phase that was also present in their samples. In our case, even if the $D0_3$ quenched phase is present in this sample, we may have missed its magnetic transition in DSC measurements owing to the baseline curvature in that temperature region. On the contrary, the $D0_3$ FM $\rightarrow$ PM transition was evident in the $M(T)$ curve, as we will discuss later. We assume that the processes detected by calorimetric measurements in Ga21 are [t21-2] and [t21-4].

DSC curves of sample Ga23 show a peak easily detected in the heating and cooling traces; the signals derivatives do not reveal additional peaks, although the signal in the high temperature portion of the derivative is quite broad and may represent convoluted processes. These processes occur at the highest temperature among the studied samples; this is consistent with the phase diagram, since on increasing Ga content the temperature of the order-disorder transformation increases, while the T_c of the A2 phase decreases, thus making processes [t21-2] and [t21-4] progressively closer until they practically coincide for $x = 22.8\%$ (see Table II). So, the signal observed in the DSC trace of Ga23 may be associated

TABLE II. List of magnetic and structural transformations for the selected compositions of Fe-Ga alloys. Transformations are listed in each column in order of increasing temperature, and labelled with an identification code [in square brackets] used as a reference in the text. FM indicates ferromagnetic phases, PM indicates paramagnetic phases; q postfix indicates a quenched, metastable phase.

Sample	**Ga 18% at.**	**Ga 21% at.**	**Ga 23% at.**
Phase composition from XRD	A2	$D0_3q$ + $L2_1$	$D0_3$ + $L2_1$
Transformations	A2 FM → A2 PM $T \approx 690$ °C [t18-1] magnetic transition	$D0_3q$ FM → $D0_3q$ PM $T = 536$ °C [t21-1] magnetic transition $D0_3$ PM → A2 FM $T \approx 600$ °C [t21-2] order-disorder $L1_2$ + $D0_3$ → $D0_{19}$ $T = 605$ °C [t21-3] reverse eutectoid A2 FM → A2 PM $T \approx 670$ °C [21-4] magnetic transition $D0_{19}$ → B2 $T = 680$ °C [t21-5] congruent reaction	$D0_3q$ FM → $D0_3q$ PM $T \approx 520$ °C [t23-1] magnetic transition $L1_2$ + $D0_3$ → $D0_{19}$ $T = 605$ °C [t23-2] reverse eutectoid $D0_3$ PM → A2 PM $T \approx 650$ °C [t23-3] order-disorder $D0_{19}$ → B2 $T = 680$ °C [t23-4] congruent reaction

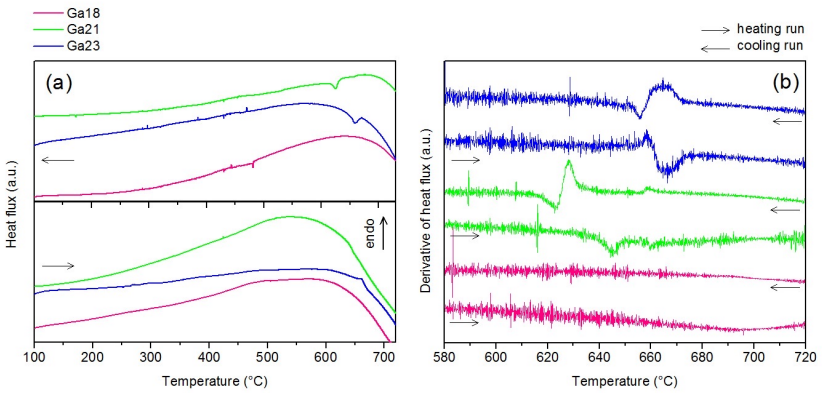

FIG. 5. DSC traces of the studied samples recorded with a temperature rate of 5 °C/min. (a) Heat flux of the first heating and first cooling segments of the measurement (the arrow represents the direction of the temperature ramp). (b) Signal derivatives in a reduced temperature range. The colours identify the samples in the same way in both graphs. The curves have been vertically translated for clarity.

to an order-disorder transformation occurring between paramagnetic phases, that will not be detected by thermomagnetic measurements.

The phase transformations occurring during annealing have therefore also been observed by means of magnetisation *vs.* temperature measurements, under an applied field of 500 Oe (50 mT), reported in Figure 6. All three samples are ferromagnetic at room temperature, and their magnetisation initially increases slightly with temperature because of the progressive increase of the magnetic permeability at the applied field value when the temperature is increased: in fact, at 500 Oe (50 mT) the samples are not saturated. Then, all samples display one or more processes where their magnetisation drops, which mark the Curie temperatures of the crystalline phases present in the samples. For the Ga18 specimen, there is one huge drop of the magnetisation at ≈ 690 °C [24, 48], whereas for the Ga21 and Ga23 samples minor drops of the magnetisation at ≈ 530 °C and ≈ 400 °C respectively are observed before the last drop at ≈ 660 °C and 490 °C respectively, indicating the presence of a minority phase whose Curie temperature is lower. For the Ga21 sample, after the first magnetisation drop with temperature, a subsequent increase is observed, clearly indicating that the phase having the lower Curie temperature is transforming into the one with the higher T_c [20]. This could be the case for the Ga23 sample as well, but the amount of the

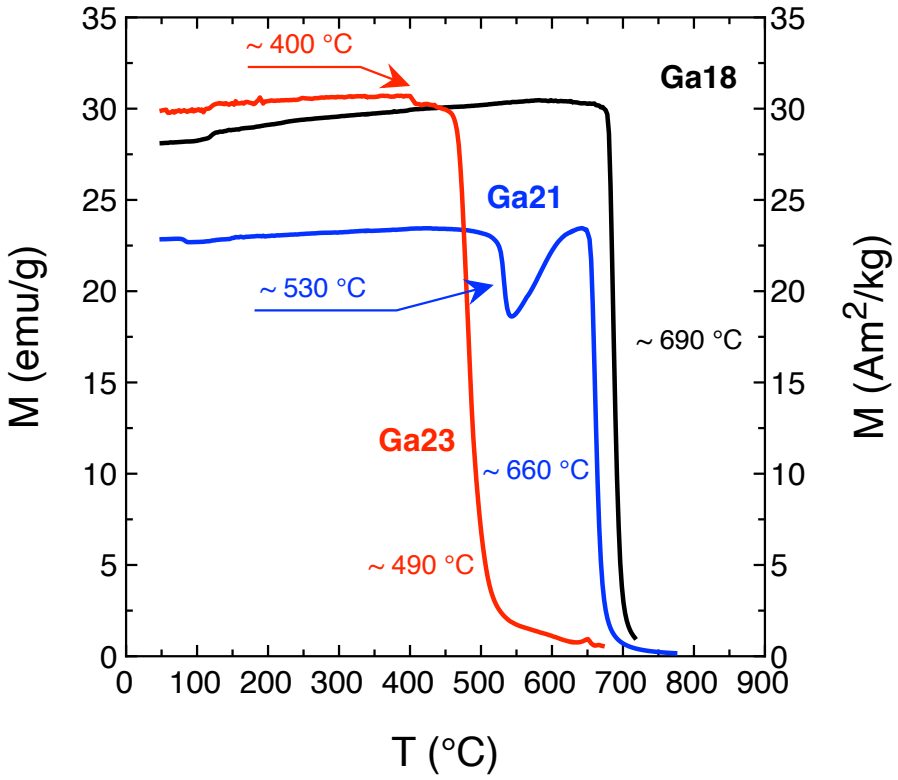

FIG. 6. Magnetisation as a function of temperature on the Ga18, Ga21 and Ga23 samples, measured under an applied magnetic field of 500 Oe.

minority phase is so small that it weakly contributes to the magnetisation signal. The Curie temperatures extracted from the curves in Figure 6 are also reported in the figure: they are in excellent agreement with the values reported in literature for similar compositions [11].

For the Ga18 sample, the $T_c \approx 690$ °C perfectly matches with the Curie temperature of the A2 phase [9, 12, 49], that is indeed the dominating one as detected by XRD and Mössbauer ([t18-1], see Table II). No phase transformations are detected during heating, in agreement with XRD and DSC data. For the Ga21 sample, the first Curie temperature at ≈ 530 °C matches very well with the FM $\rightarrow$ PM $D0_3$ transition [t21-1] [9], as also confirmed by XRD. Then, the paramagnetic $D0_3$ phase transforms into the A2 one [t21-2], giving rise to the increase of the magnetic signal at ≈ 600 °C in Figure 6, that will eventually reach its Curie temperature, slightly decreased to ≈ 660 °C [20], and in excellent agreement with DSC data [t21-4]. Finally, the Ga23 sample displays a first event at approximately 400 °C, which probably marks the overlapping occurrence of the ferromagnetic to paramagnetic transition of the $D0_3$ phase [t23-1] [9, 20], and the transformation of the $D0_3$ phase into the

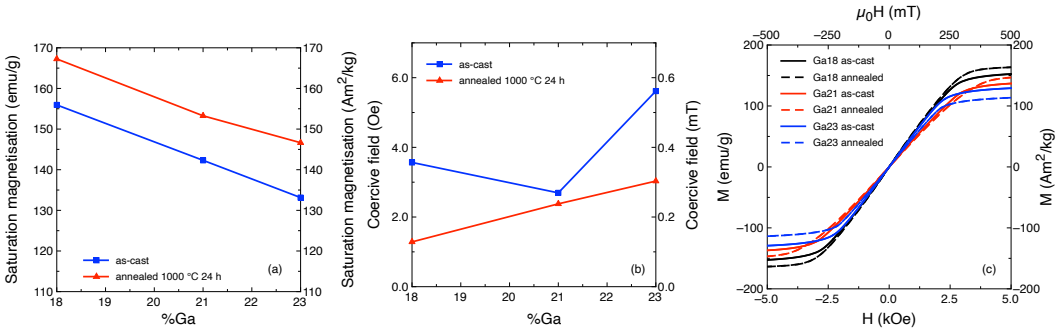

FIG. 7. (a) Evolution of the saturation magnetisation with Ga content for the as-cast and annealed (1000 °C 24 h) samples. (b) The same for the coercive field. (c) Room temperature hysteresis loops of the Ga18, Ga21 and Ga23 samples, as-cast and annealed 1000 °C 24 h.

A2 one, still ferromagnetic. Finally, the drop of the magnetisation at $T_c \approx 490$ °C marks the Curie temperature of the resulting A2 phase: in fact, the progressive decrease of the Curie temperatures of all phases in the annealed samples is due to the decrease of the average magnetic moment per Fe atom as Ga content increases [11, 45].

The effect of the annealing on the magnetic properties of the Fe-Ga alloys is shown in Figure 7. All hysteresis loops display soft magnetic behaviour, with a low-field slope that is due to the demagnetising field arising from the sample geometry and the open magnetic circuit measurement configuration (Figure 7(c)). The accurate determination of the coercive field through VSM is difficult, as H_c is of the order of the Oe (Figure 7(b)), therefore of the same order of the applied field step. With Ga content increasing, the saturation magnetisation decreases (Figure 7(a)), in perfect agreement with the literature [11, 45] (see Table III). Annealing at 1000 °C for 24 h induces the phase transformations that have been investigated through XRD, DSC and Mössbauer techniques: the overall increase of the disordered A2 phase at the expense of the ordered $D0_3$ one is accompanied by a slight increase of the saturation magnetisation [11].

Representative images of the surface magnetic domain configurations at the magnetic remanence for all the as-cast and annealed samples, acquired by magnetic force microscopy, are shown in Figure 8. Since the crystals size, as observed from electron microscopy (data not shown here), is in the $400 - 700$ μm range for all samples, the images in Figure 8 cover individual grains, except for the presence of small inclusions or precipitates which could have narrow and long shape. As a function of the Ga content, and also before and after annealing,

TABLE III. Saturation magnetisation M_S as a function of Ga content. Values marked with an asterisk * are taken from reference [45]; values marked with a double asterisk ** are taken from reference [11] and rescaled to 298 K by assuming a Langevin-type dependence of the saturation magnetisation with the $\frac{T}{T_C}$ ratio.

Ga%	M_S (emu/g) or (Am^2/kg)
0	220*
5	210*
10	195*
18	156
18	159**
20	160*
20	153**
21	142
23	133
23	131**
25	130*

there are strong variations of the domains configuration, that are a consequence of the different phases present in the samples. The Ga18 sample in the as-cast state is characterised by stripe domains, with irregular borders, more or less aligned along a common direction, that according to [8] is the local [100] direction of the A2 crystal. The irregular borders are sometimes associated to the presence of precipitates in the A2 phase [50]. Our XRD data confirm the presence of traces of the $L1_2$ phase in the predominant A2 matrix. After annealing, the irregularities on the stripes borders become so pronounced that a domain configuration starting to resemble a dendritic one appears. The presence of such features is commonly attributed to the presence of $D0_3$ or other precipitates in the A2 matrix [8, 51]; however, in our case XRD data do not reveal any significant changes in the crystal structure of the annealed sample with respect to the as-cast one, therefore this explanation must be ruled out. However, it is important to remark that the Ga18 samples display the largest magnetostriction (see below). As it has been pointed out in [52, 53], the polishing process

required to prepare the samples surface for the MFM investigations can induce an additional anisotropy term, possibly competing with the crystalline one. Artefacts in the MFM images reported in Figures 8(a,d), in the form of dendrites or stripes with irregular borders, may therefore appear, modifying at the surface the appearance of the bulk domain structure.

The as-cast Ga21 sample is characterised by a disordered magnetic configuration, with regions having a decreased contrast. Indeed, this sample consists of B2 or $D0_3$ phases, the latter along with a higher amount of the $L1_2$ phase are possibly responsible for the low-contrast areas [13, 51]. After annealing, the present phases transform into the A2 one, according to XRD and M *vs.* T measurements, giving rise to the maze- or stripe-domain structure (for the same reasons as discussed for the Ga18 sample).

The Ga23 sample in the as-cast state, instead, is mostly constituted by the $D0_3$ phase, according to XRD data. This results in a very weak magnetic contrast, with large domains [13], with small regions displaying some very disordered maze- or stripe-domains, that can be attributed to the possibly present A2 phase. After annealing, a domain configuration similar to the one of the Ga21 annealed sample develops, although with more irregular borders, compatible with the co-presence of the A2 phase with $L1_2$ precipitates, in agreement with XRD data.

All MFM images reported in Figure 8 have also been analysed by 2D-FFT, the respective results appearing in the insets. The FFTs provide a visual indication of the degree of order (or disorder) of the magnetic domain configuration of the corresponding samples. All three as-cast alloys are characterised by FFT images consisting in large halos, indicating that there is no long-range order in the domains configuration. The same applies to the Ga18 annealed sample, that even though has a slightly different domain pattern, does not display a significant evolution of its structure, as discussed earlier. Conversely, the Ga21 and Ga23 annealed samples show FFT images consisting in rings, indicating that there is a certain degree of order in the magnetic domains configuration, although isotropic, with typical features size of the order of 500 nm.

The saturation magnetostriction results are reported in Figure 9, as a function of Ga content, for both the as-cast and annealed samples. It is important to remark that the samples are polycrystalline with non oriented grains, therefore inducing magnetostrictive responses quite different from single-crystal samples [54]. The as-cast samples are characterised by lower values of magnetostriction, oscillating between 50 and 60 ppm (parts-per-million) as a

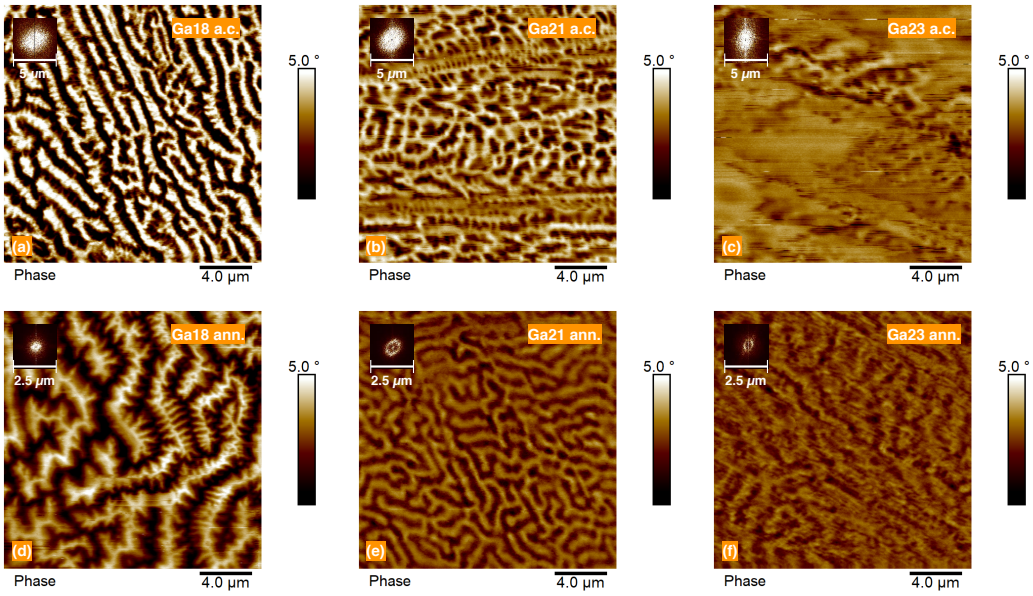

FIG. 8. MFM images at the magnetic remanence of Ga18, Ga21 and Ga23 samples in the as-cast (a.c., panels (a), (b) and (c) respectively) and annealed (ann., panels (d), (e) and (f) respectively) states. In the insets, FFT transforms of the same images.

function of the Ga content. The presence of the $D0_3$ phase at least in the as-cast Ga21 and Ga23 samples might affect this relatively low value of magnetostriction [8, 51]. After annealing, a significant increase of the saturation magnetostriction is observed for Ga18 and Ga21 samples, due to the transformation of the $D0_3$ phase into the A2 one [8]. The large increase of the saturation magnetostriction in the annealed Ga18 sample with respect to the as-cast one is noteworthy: its larger domains size should indeed favour a better magnetostrictive response [51], even though apparently the domains are less aligned along a common direction. The progressive reduction of the magnetostriction, in the annealed samples, with the Ga content, instead, is expected in this range of compositions [8].

IV. CONCLUSIONS

Fe-Ga alloys were prepared in bulk form with compositions equal to 18, 21 and 23 Ga at.%. While all three alloys already display a moderate magnetostriction in their as-cast state, annealing at 1000 °C for 24 h significantly improves the magnetostrictive response. The combined use of multiple techniques, such as X-ray diffraction, Mössbauer spectroscopy, differential scanning calorimetry, temperature-dependent magnetisation curves and magnetic

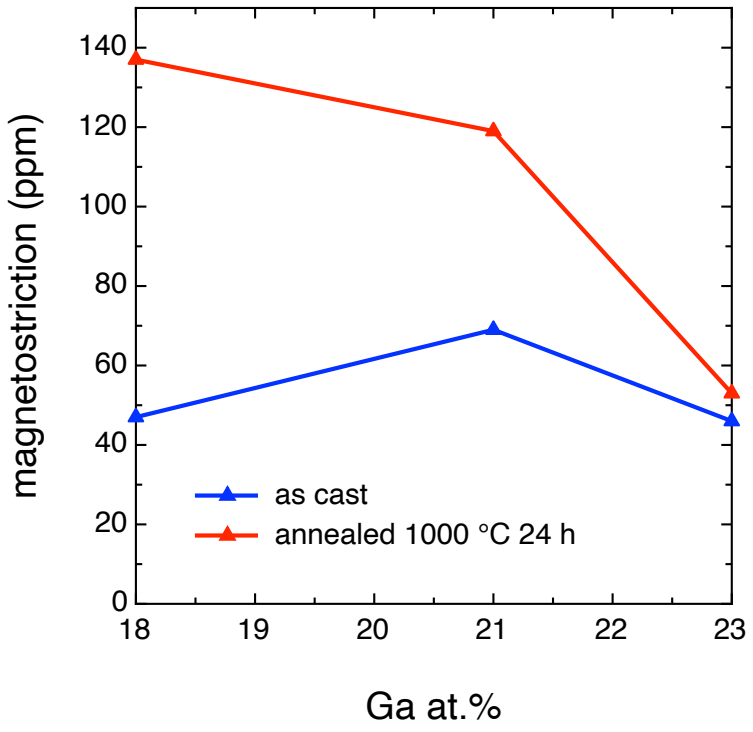

FIG. 9. Ga content dependence of the saturation magnetostriction for the as-cast and annealed (1000 °C 24 h) samples.

force microscopy allowed to assess the structure-properties relationships in the studied alloys and to evaluate the transformations occurring during annealing. As Ga content is increased, the disordered A2 phase is accompanied by the ordered $D0_3$ one, which is, however, detrimental to the development of the magnetostriction. With the high-temperature annealing, and the subsequent rapid cooling, the $D0_3$ phase transforms into the A2 one. Even if the hysteresis loops properties are not significantly affected, apart from a $\approx 5-6\%$ increase of the saturation magnetisation, the phase transformations imply profound changes in the magnetic properties, affecting the magnetic domains and the magnetostriction: the best performance is obtained with compositions close to 19%: in our case, the alloy having 18 at.% of Gallium reached almost 240 ppm of saturation magnetostriction after annealing.

With this study, we have contributed in clarifying the out-of-equilibrium Fe-Ga phase diagram in the $18-23$ Ga at.%, and the phase transformations occurring with temperature, affecting the magnetic and magnetostriction properties of the alloy.

ACKNOWLEDGEMENTS

This work has been partially performed at NanoFacility Piemonte, an INRIM laboratory supported by Compagnia di San Paolo Foundation.
The Authors would like to thank Prof. Frédéric Danoix for providing the samples which were elaborated at the ARCELOR company.

REFERENCES

[1] D.E. Parkes, L.R. Shelford, P. Wadley, V. Holý, M. Wang, A.T. Hindmarch, G. van der Laan, R.P. Campion, K.W. Edmonds, S.A. Cavill, A. W. Rushforth, *Magnetostrictive thin films for microwave spintronics*, Sci. Rep. **3** (2013) 2220, doi: 10.1038/srep02220.

[2] T. Ueno, C. Saito, N. Imaizumi, T. Higuchi, *Miniature spherical motor using iron-gallium alloy (Galfenol)*, Sensors and Actuators A **154** (2009) 92-96, doi: 10.1016/j.sna.2009.01.029.

[3] T.-D. Onuta, Y. Wang, C.J. Long, I. Takeuchi, *Energy harvesting properties of all-thin-film multiferroic cantilevers*, Phys. Lett. **99(20)** (2011) 10-13, doi: 10.1063/1.3662037.

[4] J.-M. Hu, Z. Li, L.-Q. Chen, C.-W. Nan, *High-density magnetoresistive random access memory operating at ultralow voltage at room temperature*, Nat. Commun. **2** (2011) 553, doi: 10.1038/ncomms1564.

[5] H. Ahmad, J. Atulasimha, S. Bandyopadhyay, *Reversible strain-induced magnetisation switching in FeGa nanomagnets: pathway to a rewritable, non-volatile, non-toggle, extremely low energy straintronic memory*, Sci. Rep. **5** (2016) 18264, doi: 10.1038/srep18264.

[6] D.C. Jiles, *The development of highly magnetostrictive rare earth-iron alloys*, J. Phys. D: Appl. Phys. **27** (1994) 1-11, doi: 10.1088/0022-3727/27/1/001.

[7] J. Atulasimha, A.B. Flatau, *A review of magnetostrictive iron-gallium alloys*, Smart Mater. Sctruct. **20** (2011) 043001, doi: 10.1088/0964-1726/20/4/043001.

[8] F. Bai, J. Li, D. Viehland, D. Wu, T.A. Lograsso, *Magnetic force microscopy investigation of domain structure in Fe-x at. % Ga single crystals* ($12 < x < 25$), J. Appl. Phys. **98** (2005) 023904, doi: 10.1063/1.1978971.

[9] O. Ikeda, R. Kainuma, I. Ohnuma, K. Fukamichi, K. Ishida, *Phase equilibria and stability of ordered b.c.c. phases in the Fe-rich portion of the Fe-Ga system*, Journal of Alloys and Compounds **347** (2002) 198-205, doi: 10.1016/S0925-8388(02)00791-0.

[10] *Phase diagram of binary iron alloys*, in *Monographs series on alloy phase diagrams*, vol. **9**, Edited by H. Okamoto, ASM International (1993), Materials Park, OH, USA, ISBN 978-0-87170-403-0.

[11] N. Kawamiya, K. Adachi, Y. Nakamura, *Magnetic properties and Mössbauer investigations of Fe-Ga alloys*, J. Phys. Soc. Jap. **33(5)** (1972) 1318-1327, doi: 10.1143/JPSJ.33.1318.

[12] C.J. Quinn, P.J. Grundy, N.J. Mellors, *The structural and magnetic properties of rapidly solidified* $Fe_{100-x}Ga_x$ *alloys, for* $12.8 \leq x \leq 27.5$, J. Magn. Magn. Mater. **361** (2014) 74-80, doi: 10.1016/j.jmmm.2014.02.004.

[13] I.S. Golovin, V.V. Palacheva, A. Emdadi, D. Mari, A. Heintz, A.M. Balagurov, I.A. Bobrikov, *Anelasticity of phase transitions and magnetostriction in Fe-(27-28%)Ga alloys*, Mater. Res. **21(2)** (2018) e20170906, doi: 10.1590/1980-5373-MR-2017-0906.

[14] A. Embadi, V.V. Palacheva, A.M. Balagurov, I.A. Bobrikov, V.V. Cheverikin, J. Cifre, I.S. Golovin, *Tb-dependent phase transitions in Fe-Ga functional alloys*, Intermetallics **93** (2018) 55-62, doi: 10.1016/j.intermet.2017.10.017.

[15] Y. Han, H. Wang, T. Zhang, Y. He, C. Jiang, *Exploring structural origin of the enhanced magnetostriction in Tb-doped* $Fe_{83}Ga_{17}$ *ribbons: tuning Tb solubility*, Scripta Materialia **150** (2018) 101-105, doi: 10.1016/j.scriptamat.2018.03.010.

[16] T. Zhou, Y. Zhang, D. Luan, Q. Cai, *Effect of cerium on structure, magnetism and magnetostriction of* $Fe_{81}Ga_{19}$ *alloy*, J. Rare Earths **36** (2018) 721-724, doi: 10.1016/j.jre.2018.02.004.

[17] A. Javed, T. Szumiata, N.A. Morley, M.R.J. Gibbs, *An investigation of the effect of structural order on magnetostriction and magnetic behaviour of Fe-Ga alloy thin films*, Acta Materialia **58** (2010) 4003-4001, doi: 10.1016/j.actamat.2010.03.023.

[18] G.A. Ramírez, F. Malamud, J.E. Gómez, L.M. Rodríguez, D. Fregenal, A. Butera, J. Milano, *Controlling the crystalline and magnetic texture in sputtered* $Fe_{0.89}Ga_{0.11}$ *thin films: influence of substrate and thermal treatment*, J. Magn. Magn. Mater. **483** (2019) 143-151, doi: 10.1016/j.jmmm.2019.03.099.

[19] A. McClure, S. Albert, T. Jaeger, H. Li, P. Rugheimer, J.A. Schaefer, Y.U. Idzerda, *Properties of single crystal* $Fe_{1-x}Ga_x$ *thin films*, J. Appl. Phys. **105** (2009) 07A938, doi:

10.1063/1.3077207.

[20] X. Liu, M. Li, J. Gou, Q. Li, Y. Lu, T. Ma, X. Ren, *Evidence for lattice softening of the Fe-Ga magnetostrictive alloy: stress-induced local martensites*, Materials and Design **140** (2018) 1-6, doi: 10.1016/j.matdes.2017.11.036.

[21] M. Ciria, M.G. Proietti, E.C. Corredor, D. Coffey, A. Begué, C. de la Fuente, J.I. Arnaidas, A. Ibarra, *Crystal structure and local ordering in epitaxial $Fe_{100-x}Ga_x$/MgO(001) films*, J. All. Comp. **767** (2018) 905-914, doi: 10.1016/j.jallcom.2018.07.120.

[22] A.E. Clark, K.B. Hathaway, M. Wun-Fogle, J.B. Restorff, T.A. Lograsso, V.M. Keppens, G. Petculescu, R.A. Taylor, *Extraordinary magnetoelasticity and lattice softening in bcc Fe-Ga alloys*, J. Appl. Phys. **93** (2003) 8621, doi: 10.1063/1.1540130.

[23] N Srisukhumbowornchai, S. Guruswamy, *Influence of ordering on the magnetostriction of Fe-27.5 at.% Ga alloys*, J. Appl. Phys. **92** (2002) 5371, doi: 10.1063/1.1508426.

[24] A.K. Mohamed, V.V. Palacheva, V.V. Cheverikin, E.N. Zanaeva, W.C. Cheng, V. Kulitckii, S. Divinski, G. Wilde, I.S. Golovin, *The Fe-Ga phase diagram: Revisited*, J. All. Comp. **846** (2020) 156486, doi: 10.1016/j.jallcom.2020.156486.

[25] T. Jin, H. Wang, I.S. Golovin, C. Jiang, *Microstructure investigation on magnetostrictive $Fe_{100-x}Ga_x$ and $(Fe_{100-x}Ga_x)_{99.8}Tb_{0.2}$ alloys for* $19 < x < 29$, Intermetallics **115** (2019) 106628, doi: 10.1016/j.intermet.2019.106628.

[26] Z. Nie, Z. Wang, Y. Liang, D. Cong, G. Li, C. Zhu, C. Tan, X. Yu, Y. Ren, Y. Wang, *Structural investigations of Fe-Ga alloys by high-energy x-ray diffraction*, J. All. Comp. **763** (2018) 223-227, doi: 10.1016/j.jallcom.2018.05.327.

[27] W. Lefebvre-Ulrikson, F. Vurpillot, X. Sauvage, *Atom probe tomography: put theory into practice*, Elsevier (2016), ISBN 978-0-12-804647-0.

[28] B. Gault, M.P. Moody, J.M. Cairney, S.P. Ringer, *Atom probe tomography*, Springer (2012), doi: 10.1007/978-1-4614-3436-8_6.

[29] Ivas®3.8 User Guide (2016).

[30] I.S. Golovin, A.M. Balagurov, I.A. Bobrikov, S.V. Sumnikov, A.K. Mohamed, *Cooling rate as a tool of tailoring structure of Fe-(9-33%)Ga alloys*, Intermetallics **114** (2019) 106610, doi: 10.1016/j.intermet.2019.106610.

[31] I.S. Golovin, A.K. Mohamed, I.A. Bobrikov, A.M. Balagurov, *Time-temperature-transformation from metastable to equilibrium structure in Fe-Ga*, Mater. Lett. **263** (2020)

127257, doi: 10.1016/j.matlet.2019.127257.

[32] K. Momma, F. Izumi, *VESTA 3 for three-dimensional visualization of crystal, volumetric and morphology data*, J. Appl. Crystallogr. **44** (2011) 1272-1276, doi: 10.1107/S0021889811038970.

[33] F. Richomme, A. Fnidiki, J. Teillet, M. Toulemonde, *Tb/Fe amorphous multilayers: transformations under ions irradiation*, Nucelar Instruments and Methods in Physics Research - Section B: Beam Interactions with Materials and Atoms **107** (1996) 374-380, doi: 10.1016/0168-583X(95)00795-4.

[34] J.P. Eymery, A. Fnidiki, J.P. Riviere, *CEMS as applied to implantation studies in Fe-Al 40 at.%*, Nuclear Instruments and Methods in Physics Research **209-210** (1983) 919-924, doi: 10.1016/0167-5087(83)90900-6.

[35] J. Juraszek, O. Zivotsky, H. Chiron, V. Vaudolon, J. Teillet, *A setup combining magneto-optical Kerr effect and conversion electron Mössbauer spectrometry for analysis of the near-surface magnetic properties of thin films*, Rev. Sci. Instrum. **80** (2009) 043905, doi: 10.1063/1.3121215.

[36] A. Fnidiki, F. Richomme, J. Teillet, F. Pierre, P. Boher, Ph. Houdy, *Tb/Fe multilayers: A study by conversion electron Mössbauer spectrometry and polar Kerr effect*, J. Magn. Magn. Mater. **121** (1993) 520-523, doi: 10.1016/0304-8853(93)91259-A

[37] K.M. Hamasha, I.A. Al-Omari, S.H. Mahmood, *Mössbauer and structural studies of the $Fe_2Cr_{1-x}V_x$ alloy system*, Physica B: Cond. Matter **321** (2002) 154-158, doi: 10.1016/S0921-4526(02)00842-6.

[38] A. Fnidiki, C. Lemoine, J. Teillet, *Properties of mechanically alloyed $Fe_{100-x}Cr_x$ powder mixtures: Mössbauer study*, Physica B: Cond. Matter **357** (2005) 319-325, doi: 10.1016/j.physb.2004.11.083.

[39] G. Charitou, C. Tsertos, Y. Parpottas, M. Kleanthous, C.W. Lederer, M. Phylactides, *^{57}Fe enrichment in mice for β-thalassaemia studies via Mössbauer spectroscopy of blood samples*, European Biophysics Journal **48** (2019) 635-643, doi: 10.1007/s00249-019-01389-w.

[40] E. Bill, *^{57}Fe-Mössbauer spectroscopy and basic interpretation of Mössbauer parameters*, Practical approaches to biological inorganic chemistry, (2013) 109-130, doi: 10.1016/b978-0-444-56351-4.00005-1.

[41] H.E. Stauss, *Measurement of the linear magnetostriction of hard-worked nickel*, J. Appl. Phys. **30** (1959) 1648-1650, doi: 10.1063/1.1735029.

[42] L.R. Newkirk, C.C. Tsuei, *Mössbauer study of BiF_3-type ordering in metastable FeGa alloys*, J. Appl. Pys. **42** (1971) 5250, doi: 10.1063/1.1659931.

[43] H. Cao, F. Bai, J. Li, D. D. Viehland, T. A. Lograsso, P. M. Gehring, *Structural studies of decomposition in FeÐx at.%Ga alloys*, J. All. Comp. **465** (2008) 244-249, doi: 10.1016/j.jallcom.2007.10.080.

[44] J. Boisse, H. Zapolsky, A.G. Khachaturyan, *Atomic-scale modeling of nanostructure formation in Fe-Ga alloys with giant magnetostriction: Cascade ordering and decomposition*, Acta Materialia **59(7)** (2011) 2656-2668, doi: 10.1016/j.actamat.2011.01.002.

[45] J.M. Borrego, J.S. Blázquez, C.F. Conde, A. Conde, S. Roth, *Structural ordering and magnetic properties of arc-melted FeGa alloys*, Intermetallics **15(2)** (2007) 193-200, doi: 10.1016/j.intermet.2006.05.007.

[46] F. Stein, A. Schneider, G. Frommeyer, *Flow stress anomaly and order-disorder transitions in Fe_3Al-based Fe-Al-Ti-X alloys with X=V, Cr, Nb, or Mo*, Intermetallics **11** (2003) 71-82, doi: 10.1016/S0966-9795(02)00187-5.

[47] H.W. Williams, B.L. Chamberland, *Determination of Curie, Néel, or crystallographic transition temperature via differential scanning calorimetry*, Anal. Chem. **41(14)** (1969) 2084-2086, doi: 10.1021/ac50159a056.

[48] R. Barua, P.Taheri, Y. Chen, A. Koblischka-Veneva, M.R. Koblischka, L. Jiang, V.G. Harris, *Giant enhancement of magnetostrictive response in directionally-solidified $Fe_{83}Ga_17Er_x$ compounds*, Materials **11** (2018) 1039, doi: 10.3390/ma11061039.

[49] P. Gabriela, R. Wu, R. McQueeney, *Magnetoelasticity of bcc Fe-Ga Alloys*, Handbook of Magnetic Materials **20** (2012) 123-226, doi: 10.1016/B978-0-444-56371-2.00003-9.

[50] F. Bai, H. Zhang, J. Li, D. Viehland, *Magnetic force microscopy investigation of the static magnetic domain structure and domain rotation in Fe-x at. % Ga alloys*, Appl. Phys. Lett. **95** (2009) 152511, doi: 10.1063/1.3238062.

[51] J. Zhang, T. Ma, M. Yan, *Magnetic force microscopy study of heat-treated $Fe_{81}Ga_{19}$ with different cooling rates*, Physica B **405** (2010) 3129-3134, doi: 10.1016/j.physb.2010.04.027.

[52] C. Mudivarthi, S.-M. Na, R. Schaefer, M. Laver, M. Wuttig, A.B. Flatau, *Magnetic domain observations in Fe-Ga alloys*, J. Magn. Magn. Mater. **322** (2010) 2023-2026, doi: 10.1016/j.jmmm.2010.01.027.

[53] E. Ferrara, E. Olivetti, F. Fiorillo, E. Forton, L. Martino, L. Rocchino, *Microstructure and magnetic properties of pure iron for cyclotron electromagnets*, J. All. Comp. **615** (2014) S291-S295, doi: 10.1016/j.jallcom.2014.01.217.

[54] H.D. Chopra, M. Wutting, *Non-Joulian magnetostriction*, Nature **521** (2015) 340, doi: 10.1038/nature14459.